Adhesion and Friction of Polystyrene Surfaces around T_g

Hongbo Zeng, Nobuo Maeda,† Nianhuan Chen,‡ Matthew Tirrell, and Jacob Israelachvili*

Department of Chemical Engineering, Materials Department, and the Materials Research Laboratory, University of California, Santa Barbara, California 93106

Received October 11, 2005; Revised Manuscript Received December 22, 2005

ABSTRACT: Using a surface forces apparatus (SFA), we have studied the adhesion and friction of polystyrene (PS) films on mica having various molecular weights from 580 Da ($T_g = -45$ °C) to 1300 Da ($T_g = +39$ °C) at temperatures T from 23 to 65 °C, i.e., below and above T_g. The purpose of these studies was to establish how different static and dynamic properties and surface deformations, i.e., the *contact* and *adhesion* mechanics, of detaching and shearing polymer films change as one passes through the glass transition temperature, i.e., from solidlike or glassy to liquidlike behavior. At $T > T_g$ the polymers behave like liquids, and at low detachment and shearing rates their adhesion and friction forces are accounted by their surface energy and bulk viscosity, although fingering instabilities and cavitation accompany the detachment. For the higher MW polymers (T close to T_g), the adhesion and friction forces increasingly depend on the density of chain ends at the surfaces. The adhesion hysteresis peaked close to the bulk T_g but also depended on the load, contact time, and detachment rate. Certain correlations and scaling relations were obtained. We discuss these findings in terms of the bulk and surface molecular properties of interacting polymer surfaces above and below T_g.

Introduction

We have previously studied the adhesion, adhesion hysteresis, and friction forces between glassy polymer surfaces[1,2] and found that there is an intimate correlation among these parameters. According to the so-called Johnson−Kendall−Roberts (JKR) theory, a purely elastic sphere of radius R when pressed by a load L against a flat surface of the same material of elastic modulus K and surface energy γ will have a flat contact area of radius r (see Figure 1a) given by[3]

$$r^3 = \frac{R}{K}[L + 6\pi R\gamma + \sqrt{12\pi R\gamma L + (6\pi R\gamma)^2}] \qquad (1)$$

If both the surface energy γ and the bulk elastic modulus K are nonhysteretic (reversible on loading and unloading), the loading and unloading paths are the same, and eq 1 shows that the surfaces will separate (spontaneously jump apart) at the negative load

$$L = L_{sep} = -3\pi R\gamma \qquad (2)$$

which gives the adhesion or "pull-off" force as

$$F_{ad} = -L_{sep} = 3\pi R\gamma \qquad (3)$$

Many, especially polymeric, materials are not purely elastic but viscoelastic or hysteretic, i.e., exhibiting irreversible bulk and/or surface properties. Adhesion or surface energy hysteresis is commonly defined as[4]

$$\Delta\gamma = (\gamma_R - \gamma_A) \geq 0 \qquad (4)$$

where γ_A is the advancing surface energy on loading (increasing L in eq 1) and γ_R is the receding energy on unloading (decreasing L). $\Delta\gamma$ is a measure of the energy dissipated during a complete loading−unloading cycle. For nonhysteretic surfaces, $\Delta\gamma = 0$, $\gamma_R = \gamma_A = \gamma_0$, where γ_0 is the equilibrium

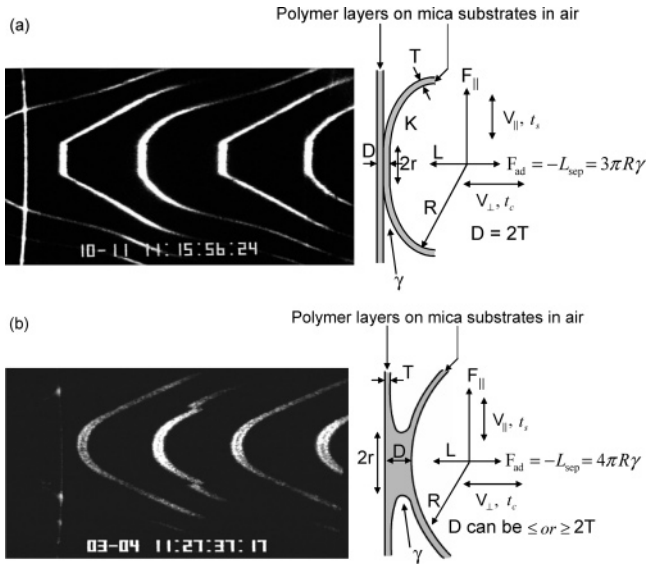

Figure 1. FECO interference fringe patterns (left) and corresponding contact geometries (right) for glassy polymer films (a), where $T < T_g$, and for melts (b), where $T > T_g$. T = initial (deposited) polymer film thickness on each mica surface, D = distance between mica surfaces as measured during experiments ($\dot{D} = dD/dt$), L = externally applied load, R = radius of (undeformed) surfaces, $2r$ = diameter of elastically flattened contact circle, where the deformation occurs mainly in the bulk material of elastic modulus K, $P = L/\pi r^2$ is the mean applied pressure, $K_\perp$ and $K_{||}$ (not shown) are the stiffnesses or spring constants of the normal and lateral force-measuring springs supporting the moving surface, which are driven at velocities $V_\perp$ and $V_{||}$, respectively (note that in general $\dot{D} \neq V_\perp$, and while the external driving velocity $V_\perp$ can be constant, $\dot{D}$ is not). γ = effective surface tension (in N/m) or surface energy (in J/m^2) of the polymer surfaces, F_{ad} = measured adhesion or "pull-off" force, γ_R = receding surface energy, t_c = waiting time at constant applied load during loading/unloading (approach/separation) experiments, and t_s = waiting time at constant applied load during shearing experiments.

* Corresponding author. E-mail: jacob@engineering.ucsb.edu.
† Current address: Department of Applied Mathematics, Research School of Physical Sciences and Engineering, Australian National University, Canberra, ACT 0200, Australia.
‡ Current address: Maxtor Corporation, Milpitas, CA 95035.

10.1021/ma052207o CCC: $33.50
Published on Web 02/16/2006

thermodynamic value, and the JKR loading and unloading paths of eq 1 are the same. When $\gamma_R \neq \gamma_A$, the receding surface energy γ_R in eq 1 should be the same as the value that gives the adhesion force F_{ad} in eq 3.[5]

Adhesion hysteresis ($\Delta\gamma > 0$) can be due to surface effects and with polymer surfaces is usually due to entanglements of chains across the contact interface.[4] But hysteresis can also arise from bulk effects due to the hysteresis in, or viscoelasticity of, the bulk modulus K in eq 1. In this case, when the separation is too rapid, the surfaces have insufficient time to peel away at the boundary, and the contact radius r does not decrease with decreasing L in the way predicted by eq 1, resulting in a (measured) adhesion force F_{ad} higher than $3\pi R\gamma_0$. Since an enhanced surface energy γ_R also causes an increased contact radius r and enhanced adhesion force, the effects of surface (γ-dependent) and bulk (K-dependent) hysteresis are often difficult to distinguish. Furthermore, in general, measured hysteretic unloading curves can no longer be fitted to the JKR equation for any values of γ_R or K, so that only eq 3 can be used, giving an "effective" surface energy γ_{eff} determined from the measured adhesion force:

$$\gamma_R(\text{non-JKR}) = \gamma_{eff} = F_{ad}/3\pi R \tag{5}$$

Experiments on a number of surfaces, including polymer,[1,2] boundary lubricant,[6,7] and inorganic surfaces,[8] have shown that the friction forces $F_{||}$ are correlated with the adhesion hysteresis, $\Delta\gamma$. Our earlier results on high-MW, high-T_g polystyrene films in the glassy state[1] showed that the most important factors that determine their adhesion hysteresis and related friction forces are due to surface rather than bulk effects, in particular the population of polymer chain ends at the surface, and their ability to interdiffuse across the interface. Thus, with decreasing MW (from a high value) both the adhesion and friction forces increase because the population of chain ends at the surface per unit area increases, as does their ability to interdigitate across the interface because of their increased mobility due to the decreasing T_g.

However, this trend with decreasing MW is not expected to continue indefinitely. With decreasing MW the T_g of the polymer eventually falls below the experimental temperature, and the polymer is no longer glassy but becomes a melt. The increased bulk fluidization of the material and mobility of the surface groups should allow for polymer chains to rapidly disentangle during a separation or sliding, resulting in an expected lowering of the adhesion and friction forces. These trends are in the opposite direction from those observed for high-MW polymers.

Theoretically, in the case of a liquid bridge between two surfaces (Figure 1b), the adhesion force is given by[9]

$$F_{ad} = 4\pi R\gamma_0 \tag{6}$$

where γ_0 is the thermodynamic surface tension of the liquid. Equation 6 has been previously verified for capillary condensed liquid bridges.[9] It differs from eq 3 by 25%, which reflects the differences between purely elastic materials and ideal liquids. As in the case of elastic contacts, deviations from ideal (thermodynamically reversible) behavior of liquids can be expressed in terms of an effective surface energy, analogous to eq 5:

$$\gamma_R(\text{nonideal}) = \gamma_{eff} = F_{ad}/4\pi R \tag{7}$$

From the above arguments, we can anticipate that the adhesion forces between (un-cross-linked) polymer surfaces should be low and similar in the limits of high and low MW, with a maximum somewhere in between.

Likewise for the shear forces. For the geometry of Figure 1b, with a liquid of viscosity η between the surfaces, the theoretical shear or friction force is[10−12]

$$F_{||} = 6\pi R\eta V_{||}[(8/15)\ln(2R/D) + O(D/R)^0]$$
$$\approx (16\pi/5)R\eta V_{||}\ln(2R/D) \quad \text{for } R \gg D \tag{8}$$

where R is the radius of the sphere and D is the closest distance of separation. For two crossed cylinders (the common geometry of SFA experiments), R is related to the cylinder radii R_1 and R_2 by[13]

$$R^2 = 2(R_1R_2)^{3/2}/(R_1 + R_2) \tag{9}$$

When $R_1 = R_2$, $R = R_1 = R_2$ and the geometry is equivalent to a sphere of radius R near a flat surface.

The maximum shear rates in a fluid for normal and shear motions of a sphere near a surface are

$$\dot{\gamma} = \frac{1}{2}\left(\frac{3}{2}\right)^{5/2}\frac{R^{1/2}}{D^{3/2}}\dot{D}, \quad \text{occurring at } r = (2RD/3)^{1/2}, \quad \text{for normal motion}^{13} \tag{10}$$

and

$$\dot{\gamma} = \frac{V_{||}}{D}, \quad \text{for shear motion} \tag{11}$$

where D is the minimum gap distance for normal or lateral (shear) motion.

Equation 8 predicts a very low value for the friction force unless D is very small (<1 nm) and/or the effective thin film viscosity η_{eff} is significantly higher than the bulk value η_0. The turnaround in the friction (and adhesion) forces is expected to occur around T_g and is the subject of this paper.

Experimental Methods and Materials

In SFA experiments the following parameters shown in Figure 1—L (or $F_\perp$), $F_{||}$, $V_\perp$, $V_{||}$, D, $\dot{D}$, R, the contact radius r, and surface geometry—can be directly measured. The typical surface geometry of two crossed cylinders was used which corresponds approximately to a sphere of radius R on a flat. Our experimental methods were the same as in previous studies.[1,2] One new feature was the use of two electric heating rods inserted into the metal walls of the SFA to allow for measurements at higher temperatures (up to 65 °C). Another new feature is the use of a beam splitter for simultaneous recording of FECO and microscope images such as those shown in Figure 6. The temperature was monitored in situ using a thermocouple. To ensure thermal equilibrium of our polymer films, 10−15 h was allowed to pass after each temperature change before any data were recorded.

Table 1 gives the properties of the polystyrene (PS) used in the experiments. The PS was purchased from Sigma-Aldrich or Pressure Chemical Co. and used as received. The glass transition temperatures (T_g) were estimated using the Fox−Flory equation[19] and/or measured by differential scanning calorimetry (DSC) at a heating rate of 10 °C/min.

Results

I. Fluid Regime ($T > T_g$). Effect of Velocity and Shear Rate on the Adhesion and Friction in the Fluid Regime. Figure 2 shows the effective (receding) surface energies for the

Table 1. Physical Properties of Polystyrene (PS) Used in the Experiments

polymer MW (Da) and polydispersity (M_w/M_n)	glass transition temp, T_g (°C)	bulk viscosity at 217 °C, $\eta_{0,217}$ (Pa s)	radius of gyration,[b] R_g (nm)	surface tension, γ_0 (20 °C)[c] (mJ/m^2 or mN/m)
PS 580 (≤1.1)	−45	<0.02	0.7	33−35[d]
PS 770 (≤1.3)	−8	<0.02	0.8	
PS 800 (≤1.3)	−3	<0.02	0.8	
PS 1240 (≤1.1)	35, 39[a]	~0.02	1.0	
PS 1300 (≤1.1)	39, 45[a]	~0.02	1.1	
PS 2330 (≤1.1)	69, 69[a]	~0.1	1.4	
PS 240 000 (~2)	106, 106[a]	7.8×10^3	13.7	37−38[d]
PS 280 000 (~2)	106, 106[a]	1.3×10^4	14.8	
PS 2 000 000 (~2)	107, 107[a]	1.1×10^7	>17	37−45[e]

[a] Measured by DSC. [b] Calculated from $R_g = 0.028\sqrt{MW}$ nm.[14] [c] $-d\gamma_0/dT = 0.058-0.077$ mN/(m deg).[15] [d] From (i) http://www.accudynetest.com/surface_energy_materials.html, (ii) http://www.sabreen.com/energies_polymers.htm, (iii) http://www.flexoconag.com/pdf/sherman/sherman/dynes.pdf. [e] From refs 16−18.

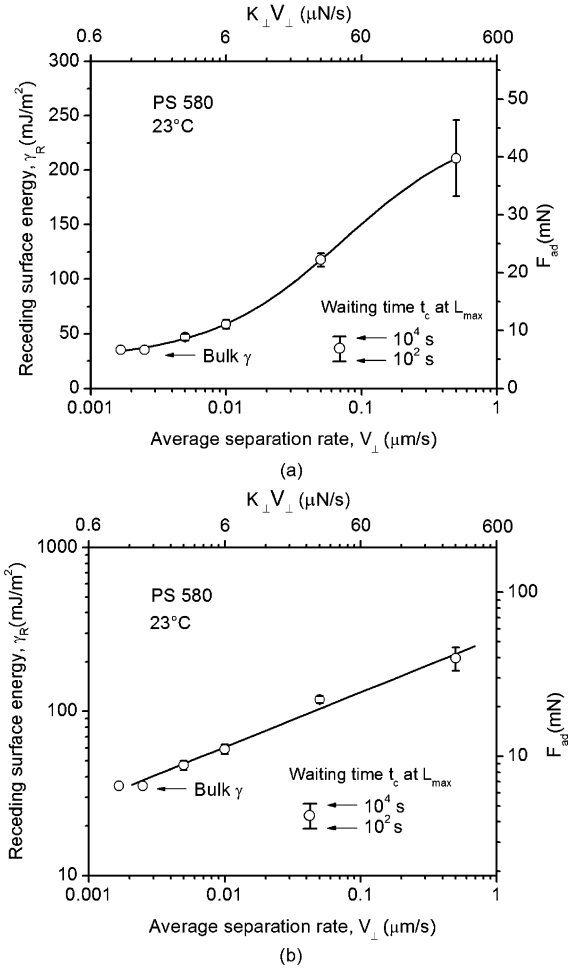

Figure 2. Receding surface energy of PS 580 as a function of average separation rate $V_\perp$ at 23 °C plotted on semilog (a) and log−log (b) scales. The surface energies γ_R (left-hand axis) were calculated from the measured adhesion or pull-off forces F_{ad} (right-hand axis) using eq 7 and $R = 2.0$ cm. The results for different contact times t_c from 10^2 to 10^4 s at the maximum load L_{max} of 30 mN (about 1−5 times F_{ad}) are represented by the vertical lines through the mean values. The top ordinate gives the rate at which the surfaces were separated in units of force per second, $dL/dt = K_\perp V_\perp$, where $K_\perp = 600$ N/m was the normal force-measuring spring stiffness. Results of similar measurements for the higher MW polymers, PS 770 to PS 1300, are described later.

lowest MW polymer (PS 580, $T_g = -45$ °C) at room temperature ($T \approx 23$ °C) as calculated from the measured pull-off forces at different separation rates and contact times. As expected, PS 580 behaves as a liquid (melt) exhibiting its thermodynamic adhesion force, or surface energy of $\gamma_0 = 33-35$ mJ/m^2, at separation rates $V_\perp$ below 0.003 μm/s (3 nm/s) or unloading force rates $dL/dt = K_\perp V_\perp$ below 2 μN/s. The adhesion force was highly sensitive to the separation rate $V_\perp$ but surprisingly insensitive to the contact time t_c at low separation rates ($V_\perp \leq 0.05$ μm/s). In both cases, however, F_{ad} increased with $V_\perp$ and t_c, as expected. Figure 2b shows that above a certain separation rate, the adhesion force or effective receding surface energy (γ_{eff} or γ_R) increases as

$$\gamma_{eff} \propto F_{ad} \propto V_\perp^{\,n} \tag{12}$$

where $n = 0.36 \pm 0.05$ under these conditions.

The shear forces $F_{||}$ with PS 580 and PS 800 (Figure 3a) were smooth (no stick−slip) and proportional to the sliding velocity $V_{||}$, again as expected for an ideal (Newtonian) liquid (cf. eq 8). Fitting the data of Figure 3a to eq 8 gave effective Newtonian viscosities of $\eta_{eff} \approx 80 \pm 50$ Pa s for PS 580 and $\eta_{eff} \approx 3350 \pm 150$ Pa s for PS 800 at 23.0 ± 0.5 °C. The bulk shear viscosities of PS 580 and PS 800 (Figure 3b) were measured using an ARES controlled strain rheometer from Rheometrics Scientific in a cone−plate geometry with 25 mm diameter and 0.1 rad cone angle. The measured shear viscosities were 230 ± 20 Pa s for PS 580 and 2800 ± 200 Pa s for PS 800, both at 24.0 ± 0.2 °C, and the fluids were Newtonian at low shear rates: $\dot\gamma < 60$ s^{-1} for PS 580 and $\dot\gamma < 10$ s^{-1} for PS 800, above which there was shear thinning. Using eq 11, the maximum shear rate in the SFA experiments (Figure 3a) fell in the bulk Newtonian regime for PS 580 only for $V_{||} \leq 10$ μm/s, above which (e.g., at $V_{||} = 27$ μm/s, when $\dot\gamma = 150$ s^{-1}) $\dot\gamma$ is in the shear thinning regime. In contrast, PS 800 in Figure 3a was always in the Newtonian regime. These considerations appear to explain the good agreement obtained for PS 800, but the lower than bulk Newtonian viscosity obtained for PS 580 in the SFA shearing experiments.

Effect of Time and Previous History. For PS 580, when the surfaces were sheared, then stopped, and allowed to remain in contact for varying periods t_s before sliding was resumed (Figure 4), no stiction spikes were ever observed. The only effect of increasing t_s is a higher friction, for example, a 50−80% increase after a contact time of $t_s = 1000$ s. This increase was due mainly to the increase in the contact area by simple flow during the stationary contact period. The results of similar stop−start experiments previously carried out with glassy high-MW PS 2 000 000 are totally different. These are also shown in Figure 4 for comparison. There are two important differences in the friction traces, which are illustrated in the insets of Figure 4: (i) with PS 580 there are no stiction spikes, while PS 2 000 000 surfaces exhibit sharp spikes and stick−slip motion; (ii) on stopping, with the liquidlike PS 580, the friction force decays rapidly to zero, as expected for a liquid, but with the glassy PS 2 000 000 the force does not relax or decay on stopping.

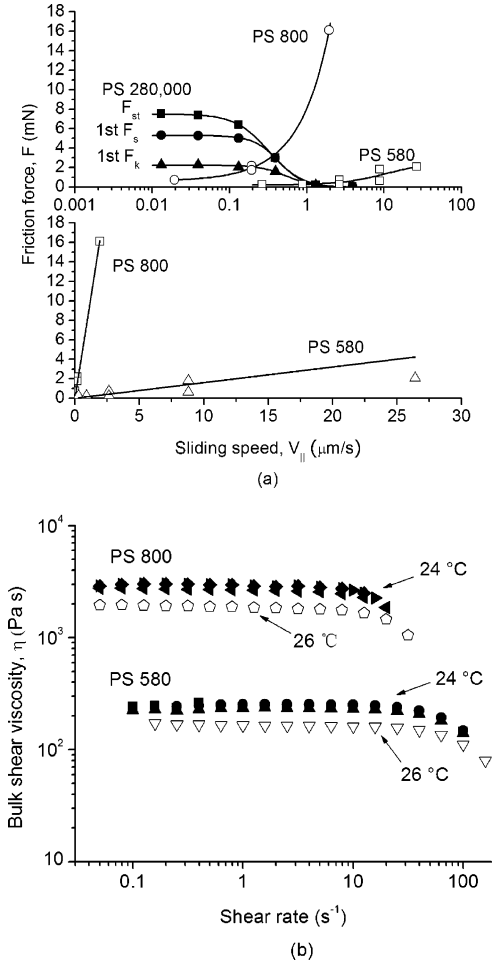

Figure 3. (a) Smooth friction forces $F_{||}$ between two adhering PS 580 layers each of thickness 90 nm ($D = 180$ nm) as a function of sliding speed at 23.0 ± 0.5 °C, with no applied load. For PS 800, $D = 165$ nm. For both polymers the friction forces increase roughly linearly with the sliding speed $V_{||}$ ($F_{||} \propto V_{||}$), as shown in the inset. Previous results for untreated glassy PS 280 000 [1] are shown for comparison. Here the friction force decreases with $V_{||}$, and there is both a stiction spike on starting (F_{st}) and stick−slip during sliding ($F_{static} > F_{kinetic}$), as usually occurs when $dF_{||}/dV_{||} < 0$. (b) The bulk shear viscosities of PS 580 and PS 800 vs shear rate, measured using an ARES controlled strain rheometer from Rheometrics Scientific in a cone−plate geometry with 25 mm diameter plate and 0.1 rad cone angle.

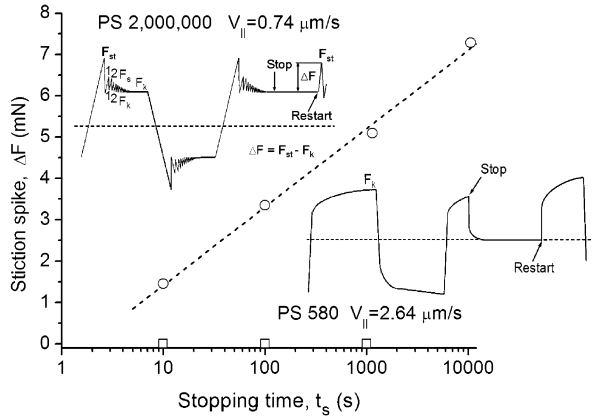

Figure 4. Stiction spikes, F_{st}, static and kinetic friction, F_s and F_k, vs stopping time t_s at $L = 0$ and 23 °C for PS 580 and PS 2 000 000 (from ref 1).

Stop−start experiments can also be done during JKR adhesion runs or cycles (some JKR plots are shown later). In these, the surfaces are compressed to a maximum load L_{max} at some steady loading rate $V_\perp$, and then, instead of immediately retracting the surfaces at the same rate, they are first allowed to relax while in contact under this load for a "contact" time t_c. Figure 5 shows some results for the three lowest MW (liquidlike) polymers PS 580, 770, and 800 as well as for the highly glassy, high MW polymer PS 2 000 000. In all cases γ_R increases with the contact time—the slope becoming steeper for the higher MW polymer, PS 800 ($T_g = -3$ °C), and less for the most fluid and most glassy polymers, PS 580 and PS 2 000 000. Thus, again we find rate-dependent effects that deviate from "ideal" behavior the closer the T_g of the polymer approaches the experimental temperature.

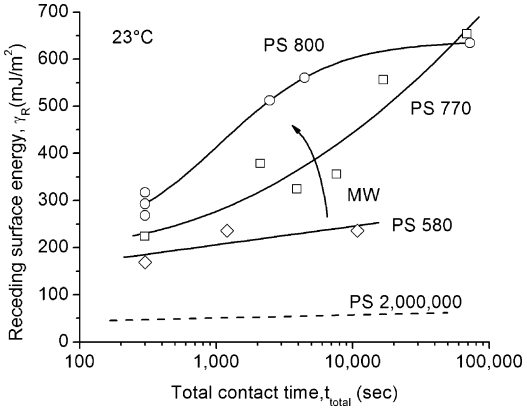

Figure 5. Receding surface energies of PS 580, 770, and 800 as a function of total contact time t_{total}, measured at a fixed separation rate of $V_\perp = 0.5$ μm/s at 23 °C. The results of similar measurements with PS 2 000 000 are also shown for comparison (from ref 1). The increased adhesion with contact time is due mainly to the increased contact area with time driven by the attractive capillary force or negative Laplace pressure within the film. The increased contact area with time can be visualized with the FECO fringes (see Figure 6).

Effect of Maximum Load during Loading−Unloading Cycles. However, unlike in the case of shearing, comparing measured time-dependent normal forces with theory is more difficult. In the case of shearing, the meniscus or capillary bridge geometry (Figure 1b) does not change substantially during the lateral motion, so that all the measurable parameters in eq 8 remain constant during steady-state sliding, allowing the effective viscosity, η_{eff}, to be calculated. This is not the case during loading or unloading where neither the local geometry nor the relative velocity of the surfaces $\dot{D}$, is constant (even if the driving velocity $V_\perp$ is constant); i.e., there is no "steady state" during a separation. The various changes occurring at a contact junction during loading and unloading of a polymer near T_g are now described in detail.

Figure 6 shows how the local geometry of a junction changes with time during rapid loading, followed by contact at constant load L_{max}, and slow unloading for two PS 1300 layers at a temperature slightly above T_g. Twenty stages of the process are shown in panels a−t and described in the figure legend. The corresponding surface separation vs time is given in Figure 7. After the surfaces detached, the craterlike deformations remaining on each surface (Figures 6t and 7t) did not relax back to a smooth profile even after 2 days at 51 °C. On bringing the two surfaces back into contact at their original locations, multiple bridges formed that coalesced into a single capillary bridge within ~20 min (not shown). Qualitatively similar results were obtained with all the polymers studied, from PS 580 to PS 1300. Fingering instabilities and cavitation were observed in all cases—the main differences were the different times needed for the different stages.

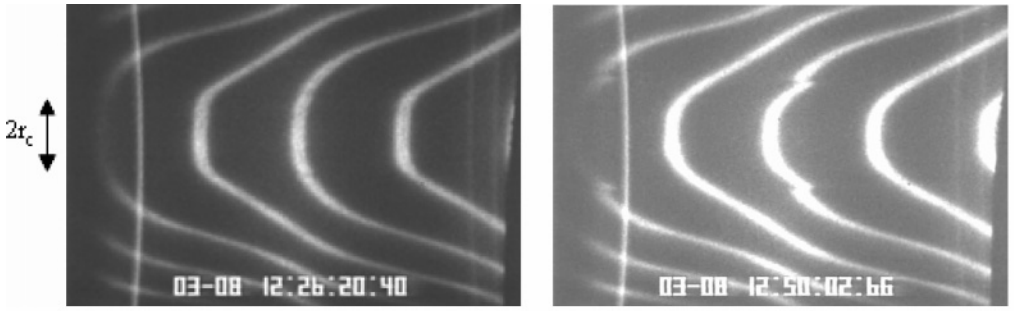

(a) Beginning of waiting at L_{max} (t_c= 0 sec), D_0=160 nm. (b) t_c= 23 min 43 sec.

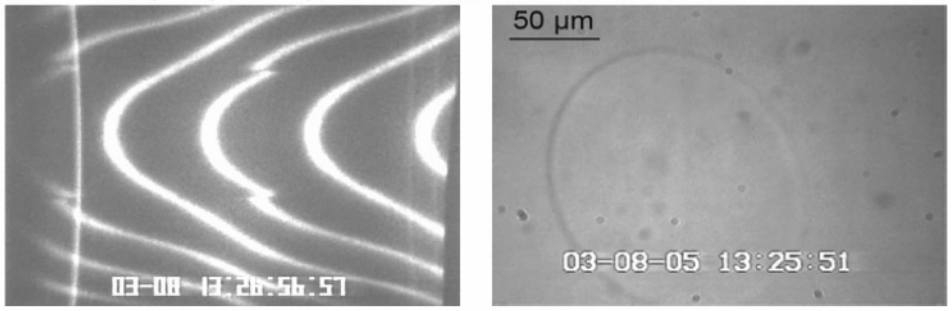

(c) Start of separation after a total wait of t_c=1 hr at L_{max}, t = t_c + 36 sec, D=108 nm.

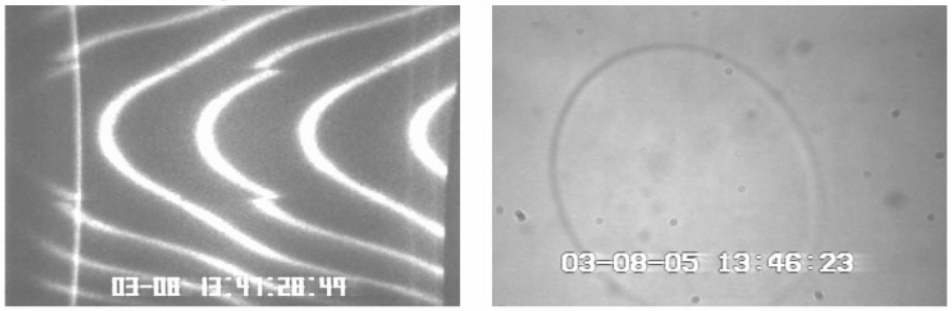

(d) t = t_c + 21 min 8 sec, D=100 nm.

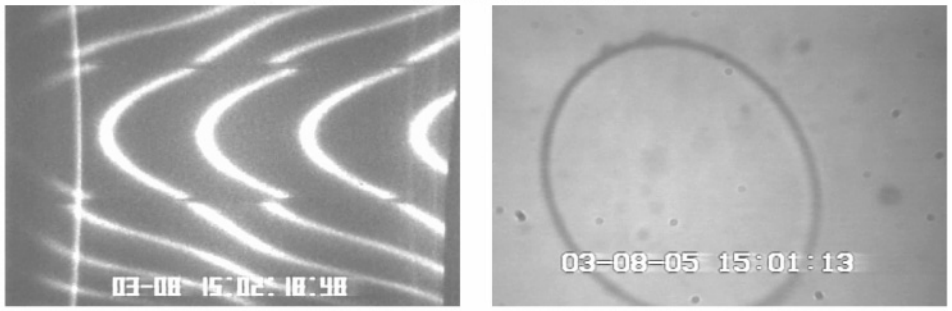

(e) t = t_c + 1 hr 35 min 58 sec.

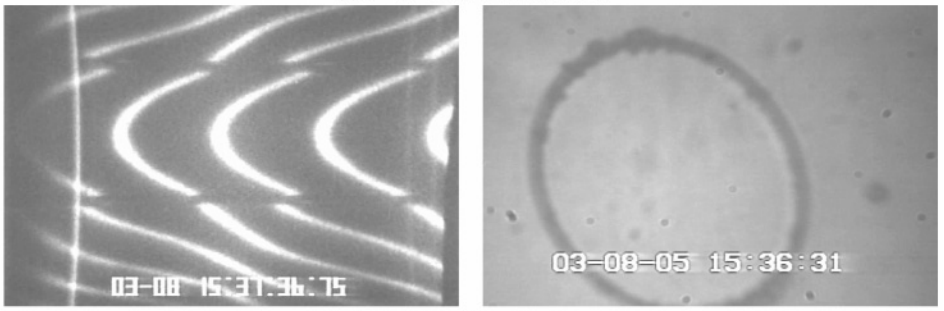

(f) t = t_c + 2 hrs 11 min 16 sec.

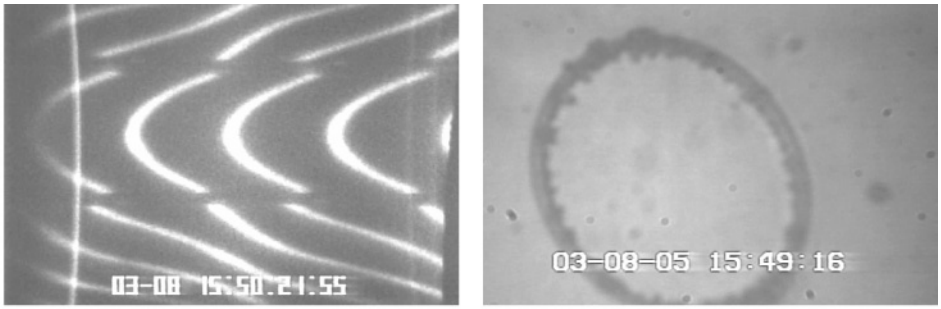

(g) Start of fingering (Saffman-Taylor instability), $t = t_c + 2$ hrs 24 min 1 sec.

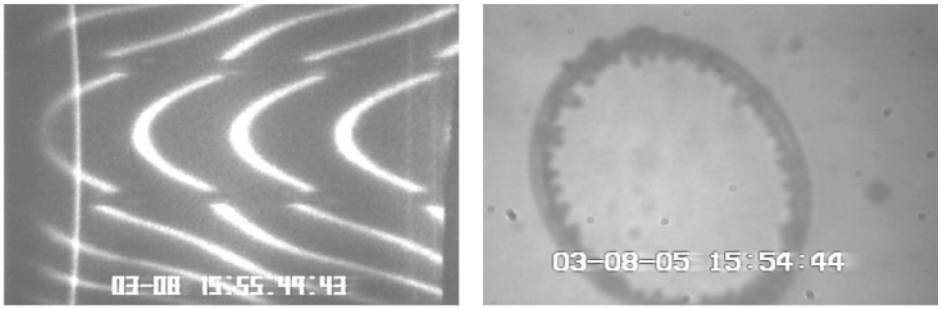

(h) Surfaces start to move slowly apart, $t = t_c + 2$ hrs 29 min 29 sec.

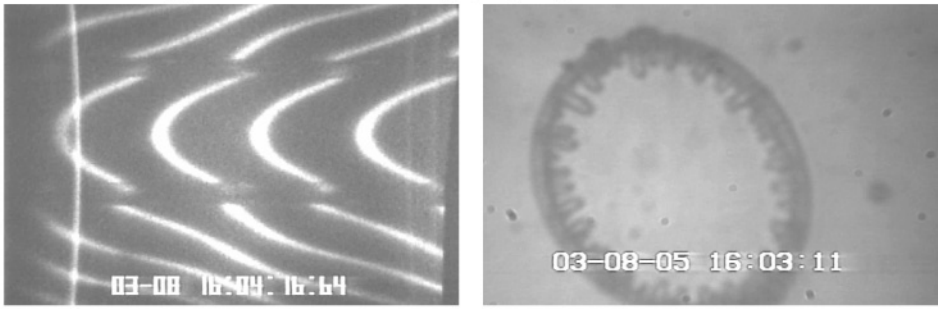

(i) Surfaces move apart more rapidly (start of pull-off jump), $t = t_c + 2$ hrs 37 min 56 sec.

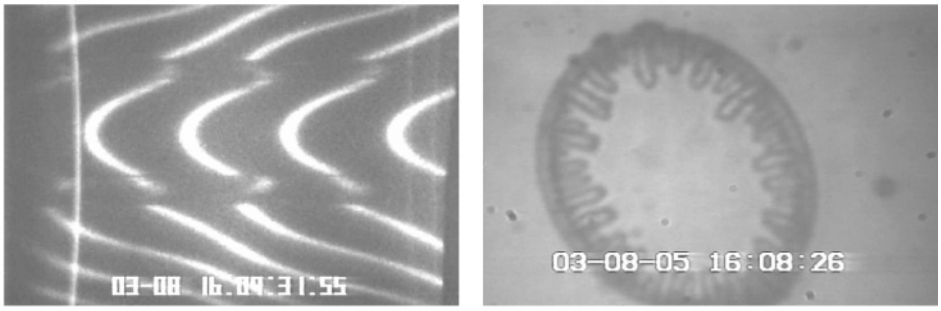

(j)

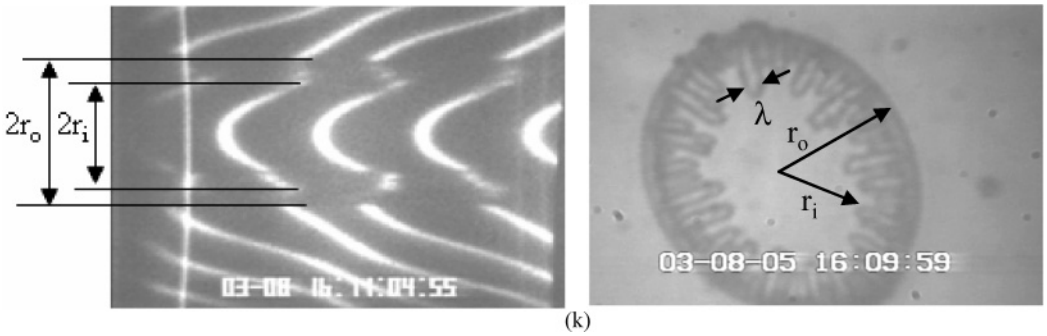

(k)

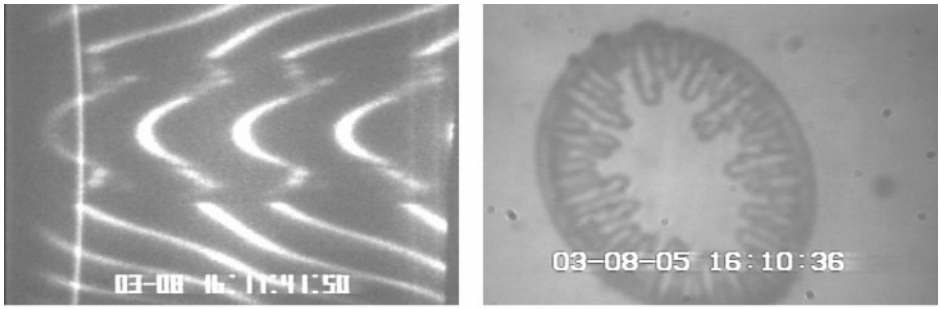

(l)

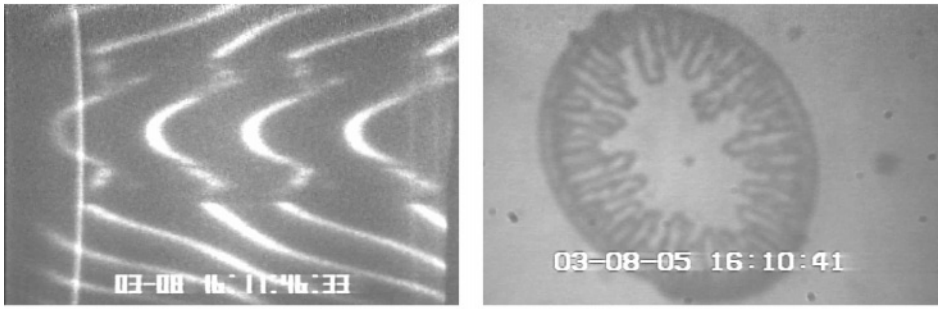

(m) Cavitation starts near the center, $t = t_c + 2$ hrs 45 min 26 sec.

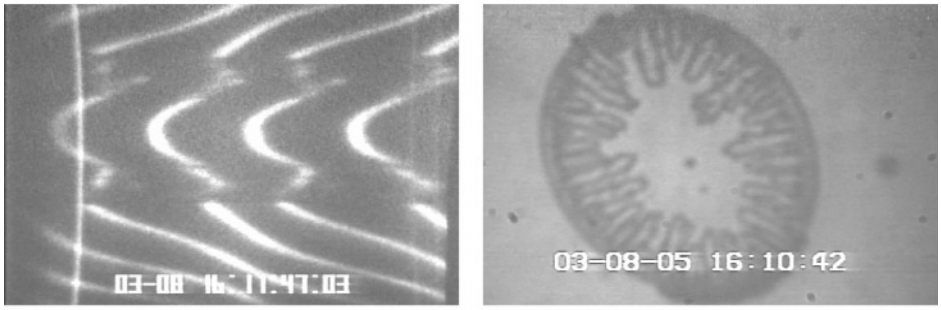

(n)

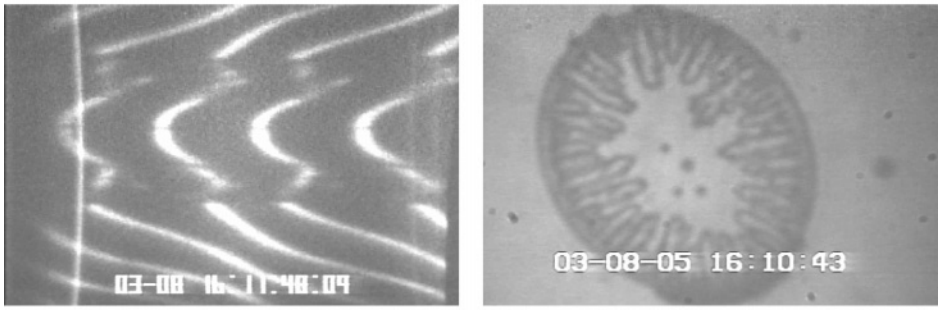

(o) Cavitation bubbles continue to grow even away from the center.

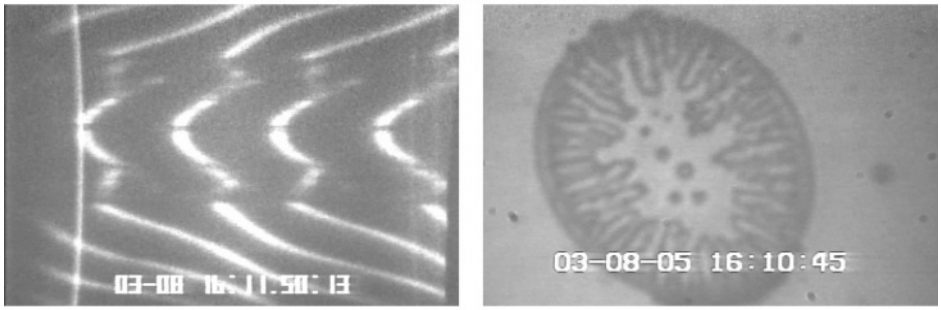

(p)

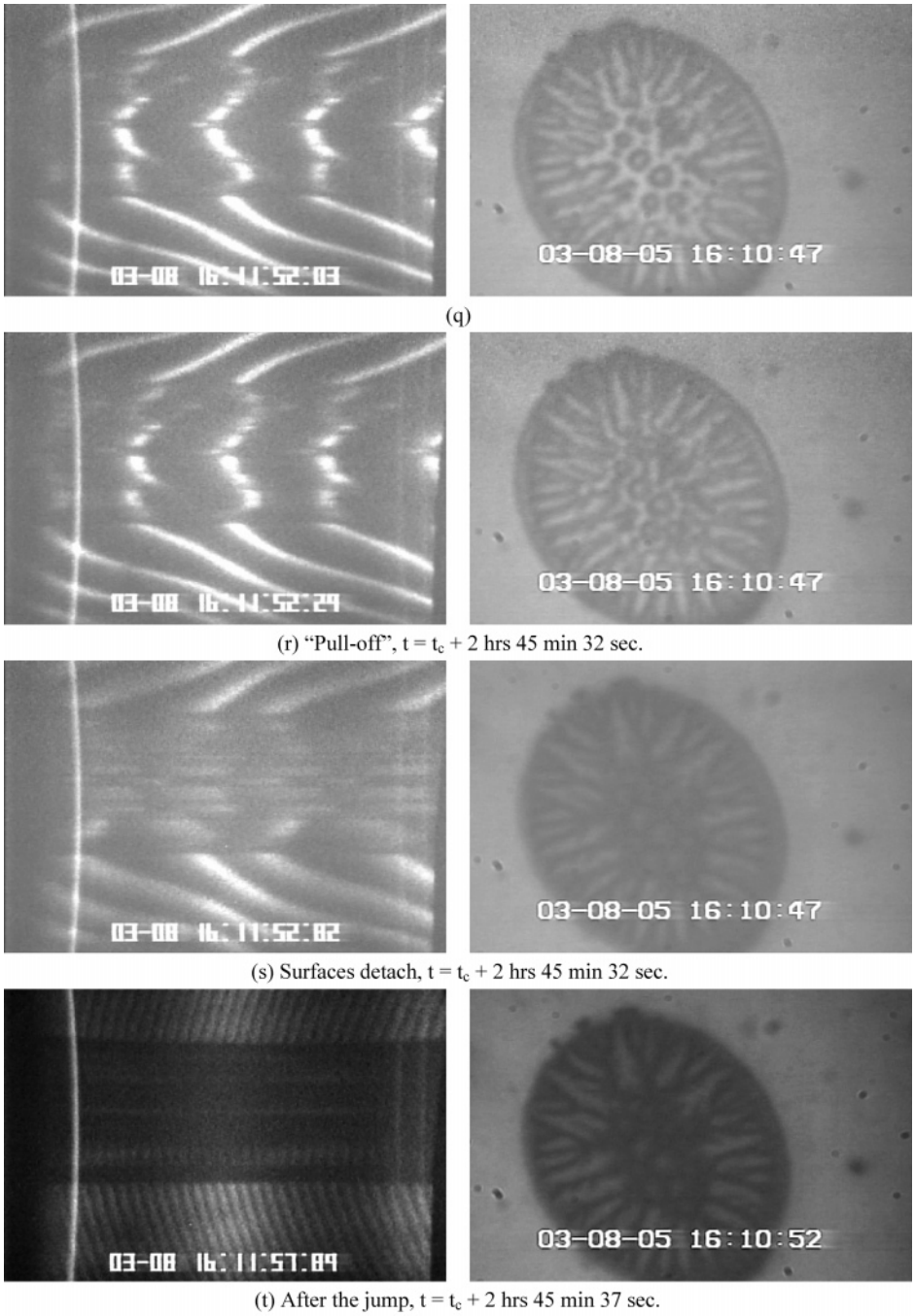

Figure 6. FECO fringes (left) and optical microscope views (right) of two PS 1300 layers of initial thickness $T = 80$ nm at 51 °C (cf. $T_g = 39-45$ °C) as a function of time. Panel (a) defines $t = 0$: the surfaces have just been brought into flattened contact at a rapid rate of 0.5 μm/s to a load of $L = L_{max} = +30$ mN. (b) Growth of capillary bridge seen as a break in the even fringes (which are sensitive to changes in the refractive index). (c) Commencement of separation after a contact time of $t = t_c = 1$ h at $L = L_{max}$. Driving velocity of separation: $V_\perp = 0.017$ μm/s, which remained constant until the surfaces finally separated at (s). (d)−(e) Surfaces still move toward each other and contact area increases until $L = 0$, after which $L < 0$ and the surfaces begin to move away and the contact area begins to fall. (g) Start of inward fingering. (j)−(l) Rapid increase in rate of mica−mica surface separation $\dot{D}$, tending to an instability or jump apart, but with the polymer still bridging the surfaces. (m) Start of cavitation bubbles within the polymer bridge. (s) Polymer bridge snaps, surfaces jump apart. (t) Surfaces come to rest after jumping apart. The whole process took 2 h $45^1/_2$ min. [Note: the FECO and microscope camera times were offset by 1 min 5 s.]

Figure 8 gives the "JKR plots" for PS 1300 on loading and unloading after different contact times t_c at the same maximum load of $L_{max} \approx 30$ mN. The top two curves (points ◆ and ◇) correspond to the results of Figures 6 and 7, i.e., for a contact time of 1 h. As can be readily seen, while the rapid loading curve (points ○) follows the JKR theory, eq 1, reasonably well, and there is no fingering,[47] the receding curves do not follow the JKR equation at all: there is a pinning of the circular outer boundary (r_o), and the decrease in the contact area (r_i) occurs via an inward fingering process. Note, too, the continually increasing contact area with time at the fixed load L_{max}.

Figure 9 shows the complex relationships between some of the dynamic parameters associated with each separation process. For the geometry of a sphere near a flat surface (or two spheres) neither the shear rate $\dot{\gamma}$ nor the Deborah number De is uniform throughout the liquid between the surfaces. We therefore plot the maximum values of $\dot{\gamma}$ and De at any time during each separation process, showing how they vary with D, $\dot{D}$, $V_\perp$, and

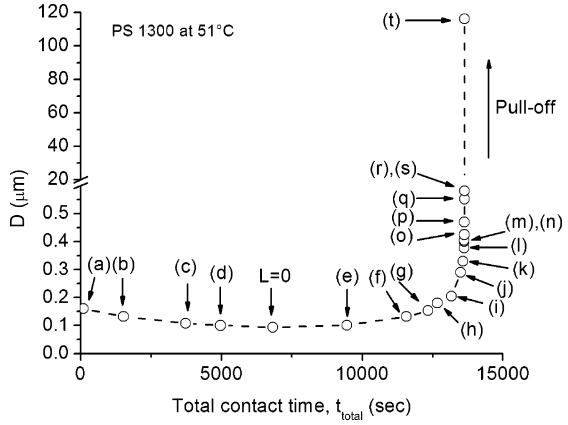

Figure 7. Minimum gap distance D vs total contact time t_{total} corresponding to the panels of Figure 6.

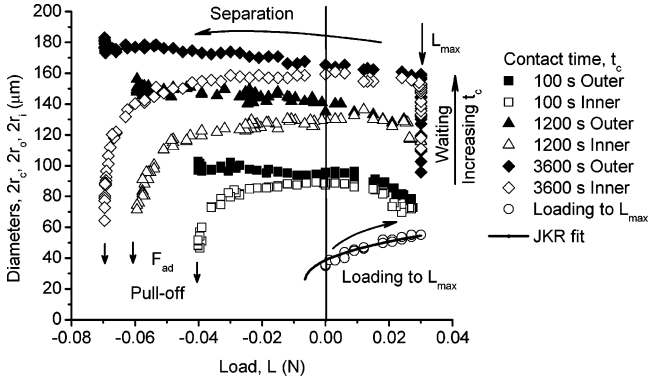

Figure 8. "JKR plots" of initial loading curve (○) and various unloading curves for PS 1300 at 51 °C for three different contact times t_c between 100 and 3600 s, all at the same maximum load of L_{max} = 30 mN. The unloading curves give the outer and inner radii of the contact junctions, r_o (■, ▲, ◆) and r_i (□, △, ◇), as defined in Figure 6, panel k.

$F_\perp$. The maximum values in these plots are therefore the maxima of the maximum values, while the maximum value of $F_\perp$ is the pull-off or adhesion force, F_{ad}. Figure 9a shows the normal force $F_\perp$ and maximum force F_{ad} as a function of the separation distance D corresponding to Figures 6 and 7 and the top two curves (points ◆ and ◇) of Figure 8. Figure 9b,c shows the relationships between the maximum shear rate $\dot{\gamma}$ and Deborah number De during separation vs the force $F_\perp$, the intersurface separation distance D, and separation velocity $\dot{D}$. The maximum shear rate is defined by eq 10 and the Deborah number by eq 13 after Shull and Creton,[20] viz., the real strain rate multiplied by the relaxation time of the polymer τ at the experimental temperature:[48]

$$\mathrm{De} = \tau \frac{\dot{D}}{D} \tag{13}$$

From the previous study by Santangelo and Roland,[21] τ for PS 1300 at 51 °C can be estimated to be in the range 0.001−0.1 s, and we here assumed that τ = 0.01 s. Figure 9d shows De at the maximum pull-off force F_{ad} at the four different separation velocities (shown in Figure 10) and the maximum De during each separation. Note that maximum De does not occur at maximum $F_\perp$.

Figure 10 shows further details of the receding surface energy of PS 1300 at 51 °C (a few degrees above T_g). The lines in Figure 10b are linear on a log−log plot, following eq 12: $\gamma_R \propto V_\perp^n$, with exponents n between 0.15 and 0.26 (n increasing with t_c). When extrapolated back, the lines cross at roughly γ_R = 55 ± 25 mJ/m^2 (cf. γ_0 = 33−38 mJ/m^2) when $V_\perp = 10^{-6}$−10^{-5} μm/s (0.01−0.1 Å/s). These results may be compared with those for PS 580 at 23 °C (∼70 °C above T_g) where the thermodynamic surface energy γ_0 was reached at a separation velocity of 0.003 μm/s or 30 Å/s (Figure 2b). With PS 1300 at 51 °C, with the force-measuring spring of stiffness $K_\perp$ = 600 N/m used in these experiments, the surfaces would have had to be separated at ∼0.1 Å/s for ∼100 days to reach thermodynamic (fluidlike) pull-off.

II. Transition Regime ($T \approx T_g$) and the Glassy Regime ($T < T_g$). Effect of Temperature: Passing through T_g. As discussed in the Introduction, we expect nonideality or energy dissipation to peak somewhere around T_g. To test the effects of "passing through T_g", adhesion measurements were made with PS 1240 (T_g = 35−39 °C) and PS 1300 (T_g = 39−45 °C) at different separation rates and temperatures in the range 23−65 °C.

At the lower temperatures, these polymers exhibited behavior similar to glassy PS as previously found[1] for molecular weights from 1300 to 2 × 10^6. Our results for two PS 1300 layers are shown in Figure 11. Figure 11a shows the receding surface energy γ_R as a function of temperature, measured immediately after the surfaces came into contact, L_{max} = 0 (at a low separation velocity of $V_\perp$ = 0.005 μm/s and a stiff spring of $K_\perp$ = 3100 N/m). There is a peak in γ_R,[49] which occurs close to 40 °C. At low temperature (24 °C), the surface energy approaches the thermodynamic value. Figure 11b shows γ_R as a function of separation rate $V_\perp$ at different temperatures. Figure 11c shows that for L_{max} = 30 mN, γ_R increases faster with t_c at higher temperatures. Figure 11 therefore shows that the conditions of maximum adhesion hysteresis is determined by more than just the temperature, but also by $V_\perp$, t_c, and L_{max} (discussed further below). Similar results (not shown) were obtained for PS 1240 layers of thickness T = 30 nm. For PS 1240 compressed to L_{max} = 30 mN and then separated at $V_\perp$ = 0.5 μm/s, γ_R remained low until 43 °C, above which it increased up to 53 °C—the highest temperature measured. This is 15 °C above T_g.

It is apparent from Figure 11 for PS 1300, and the similar results obtained for PS 1240, that maximum adhesion hysteresis can occur 10−25 °C above T_g depending on the experimental conditions, viz., the thickness of the polymer layers T (here ∼30 nm), the compressive load L_{max} (here ∼30 mN, which corresponded to maximum applied pressures, as defined in Figure 1, of $P = L_{max}/\pi r^2$ = 25−40 atm), the separation rate $V_\perp$ (here varied between 0.005 and 0.5 μm/s), and the contact time t_c (here varied from 300 to 10^5 s).

Pressure is known to affect the viscoelastic properties of polymers and is a parameter in the WLF equation.[22] We found that the maximum applied load L_{max} or pressure in our JKR experiments affects γ_R and the adhesion hysteresis. Most of the results shown so far were for large applied pressures of 25−40 atm. For lower loads and pressures the peaks occurred at lower temperatures, and for $L_{max} \approx 0$, corresponding to purely self-adhesive contacts, these fell to around/below the bulk T_g (cf. Figure 11a,b).

Finally, we reiterate that all of these complex effects are not occurring across a uniform polymer film: the physical conditions and surface and film geometry are continually changing in different ways at different locations of the junction. Figure 12 shows the type of deformations occurring and the likely flow lines within the polymer "films" during a loading and unloading cycle. In particular, the separation mechanism, involving viscous fingering, must play an important role in any theoretical analysis of the results.

CDV

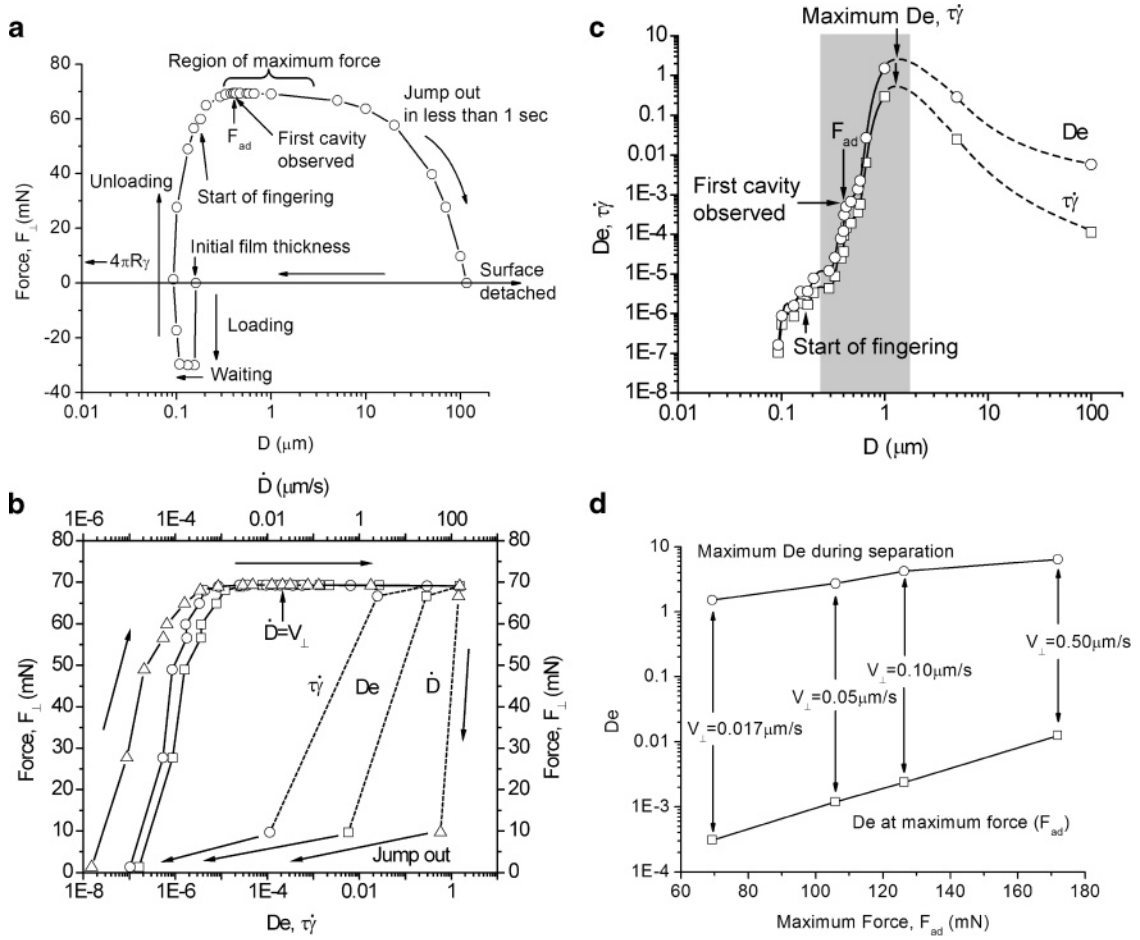

Figure 9. Relationships between the measured forces $F_\perp$, separation distance D, separation velocity $\dot{D}$ (included in De via eq 13), and shear rate $\dot{\gamma}$ during the separation processes shown in Figures 6 and 7 and the top two curves in Figure 8. (a) Force vs separation distance. (b) Force vs De, $\tau\dot{\gamma}$ and $\dot{D}$ during separation. (c) De and $\tau\dot{\gamma}$ vs separation distance during the separation; the gray band is the maximum force regime. Dashed lines in (b) and (c) just before detachment (jump out) are of uncertain magnitude. (d) The maximum De vs maximum forces during each separation (at different $V_\perp$) taken from Figure 10, and De at the maximum force, F_{ad} (lower curve).

Analysis and Discussion

New Scaling Relations. Our results reveal some new scaling relations for the dynamic adhesion forces F_{ad} and surface energies γ_R (which are linearly related via eq 7) of polystyrene well below the bulk T_g to about 10 °C above T_g. Thus, for different separation or pulling rates $V_\perp$, we find that above some critical value, $\gamma_R \propto V_\perp{}^n$, where $n = 0.15-0.36$.[50] A power-law dependence was also found for the contact time t_c, $\gamma_R \propto t_c{}^n$, with $n = 0.16-0.26$. These scaling relations may also be compared with previous work by Muller,[23] Li,[24] and Barthel and Roux[25] on the dynamic adhesion energies during tape peeling, who found n to be in the range 0.1−0.8. However, it should be noted that in their studies the velocity was the crack tip velocity rather than the separation velocity $V_\perp$ as measured here. Francis and Horn[26] have made theoretical predictions about the relationship between purely viscosity-determined pull-off forces and the pulling rates $V_\perp$ for a sphere and a planar surface (or two detaching spheres) with a liquid bridge between them, which also predicts a power-law dependence but with an exponent n of about 0.5. The reason for the differences between our experiment ($n = 0.15-0.36$) and the theoretical prediction is discussed below.

Maximum Dissipation in Relationship to the Bulk T_g of Polystyrene. Figure 13 shows generic plots for the maxima in the adhesion hysteresis, $\Delta\gamma = (\gamma_R - \gamma_A) \approx \gamma_R$, and friction forces, F_{ll}, based on Figure 11 for PS 1300 and the other figures for the lower MW PS. Concerning the location of the peaks relative to the bulk T_g, at low or zero loads, L, the adhesion hysteresis of thin films of PS 1240 and 1300 peaked at or slightly below T_g, while at high loads the peak shifted to several degrees above T_g. Figure 13 is a WLF-like representation[22] where the velocity and load may be thought of as representing the frequency and pressure, respectively, in bulk rheological measurements.

Adhesion and Friction Dissipation Mechanisms. The results of these and previous SFA experiments[1,2] on polymer−polymer adhesion and friction suggest that the adhesion hysteresis and friction of un-cross-linked homopolymers are governed by two different mechanisms: (i) the surface density of chain ends that can interdigitate across the contacting interface and (ii) the bulk viscoelasticity of the polymer that determines its viscous and capillary forces. For low-MW polymer, e.g., PS 580 which contains only 5−6 segments, these two effects may merge, but for higher molecular weights they become more distinct and could give rise to two peaks in adhesion and friction plots such as those shown in Figure 13.

Glassy PS (high MW, $T < T_g$) exposes mostly loops with few chain ends at the surfaces. The loops have very long relaxation times, and the bulk viscosity is very high. Adhesion hysteresis and friction are low and are mainly due to a few short chain ends and loops interdigitating between the surfaces. There is no bulk flow, and the surfaces behave like elastic solids (elastomers). The contact mechanics follows the JKR theory, and the adhesion force is given by $F_{ad} = 3\pi R\gamma$. These are the

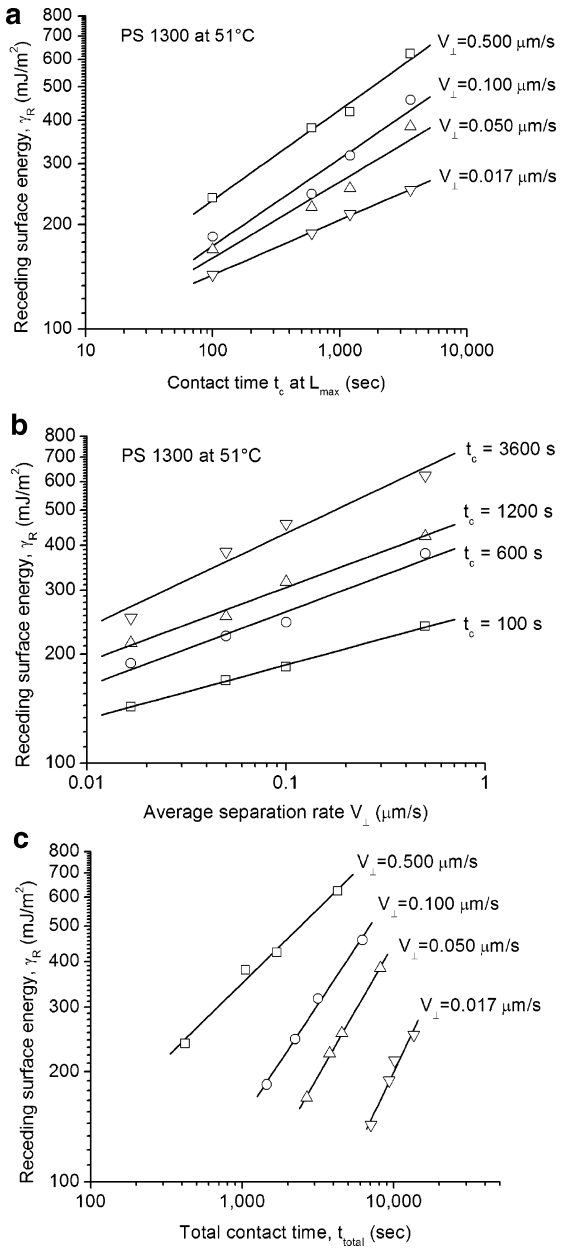

Figure 10. Receding surface energy for PS 1300, as defined by eq 7: $\gamma_R = F_{ad}/4\pi R$, at different separation rates $V_\perp$ and contact times t_c at $L_{max} = 30$ mN, all measured at 51 °C. The left-most column of points in (b) correspond to the JKR plots shown in Figure 8. (a) γ_R vs t_c at different $V_\perp$; (b) γ_R vs $V_\perp$ at different t_c. (c) γ_R vs total contact time at different $V_\perp$.

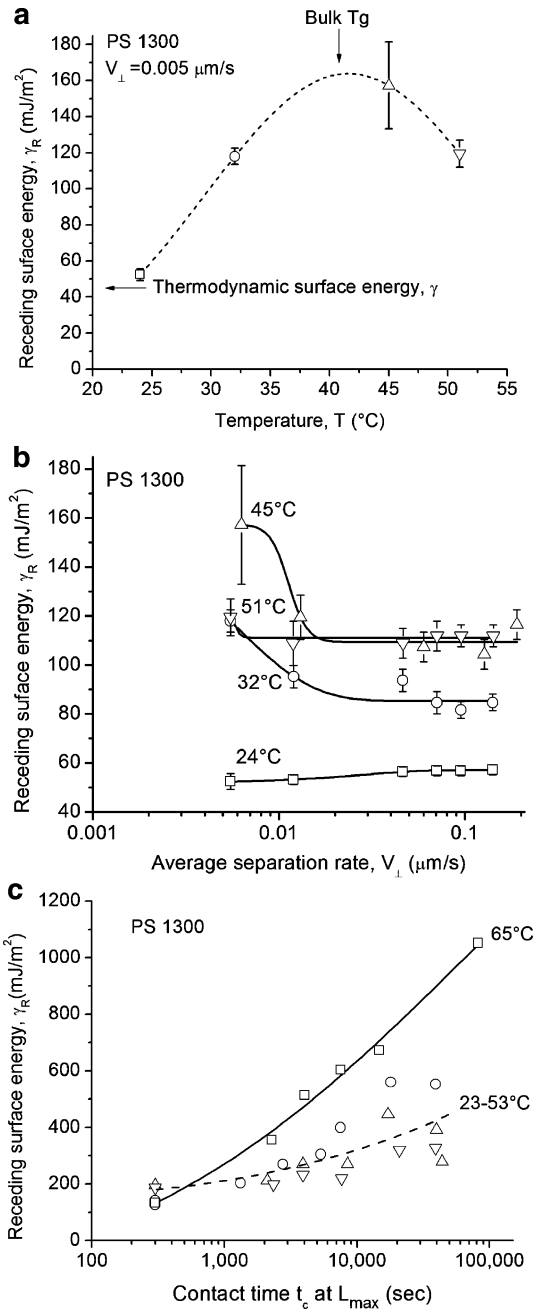

Figure 11. Receding surface energies of two PS 1300 layers at (a) different temperatures at the same separation rate of $V_\perp = 0.005$ μm/s ($T = 90$ nm), (b) different separation rates at different temperatures ($T = 90$ nm), and (c) contact times ($L_{max} = 30$ mN, $T = 32$ nm). $L_{max} = 0$ mN in (a) and (b). Other experimental variables and fixed conditions are given in each panel. As T falls, the adhesion mechanism (or "contact mechanics") changes from liquidlike (Figure 1b) to JKR solidlike (Figure 1a), and we have consequently changed the calculation of γ_R from eq 7 to eq 5 in going from 65 to 23 °C.

"solidlike" regions in Figure 13. However, if there is a high density of short, mobile end groups at the surfaces, for example, due to branching or cross-linking followed by bond-breaking of the surface bonds, both the adhesion hysteresis and friction will be enhanced due to this purely surface effect.

At the opposite extreme of "liquidlike" polymer (low MW, $T > T_g$), these expose both ends and loops in the bulk and at the surface, where both have short relaxation times and where the bulk viscosity is low. JKR-type contact mechanics does not hold: the deformations are large and are described by the geometry of the deforming surfaces involving macroscopic flow both on approach and separation. In the "thermodynamic" limit (see Figure 13) the adhesion is determined by the thermodynamic γ because there is time for both the ends and loops to entangle and disentangle during a loading and separation, and the adhesion force is given by $F_{ad} = 4\pi R\gamma$. Thus, we have the same (or almost the same) adhesion as in the elastic (glassy) limit but for very different reasons and based on very different contact mechanics. (We may note that the elastic limit is very far from thermodynamic equilibrium.)

Concerning where the transition from one type of behavior to the other occurs, for the higher MW PS 1240 and 1300 used in this study at $T < T_g$, the adhesion hysteresis was comparable to that previously found for PS 2330 under similar loading−unloading conditions.[1] This suggests that the adhesion hysteresis of PS 1240 and 1300 at temperatures of 20 °C or more below T_g is already governed by the same mechanism that governs higher MW PS surfaces: the chain ends at the surfaces which

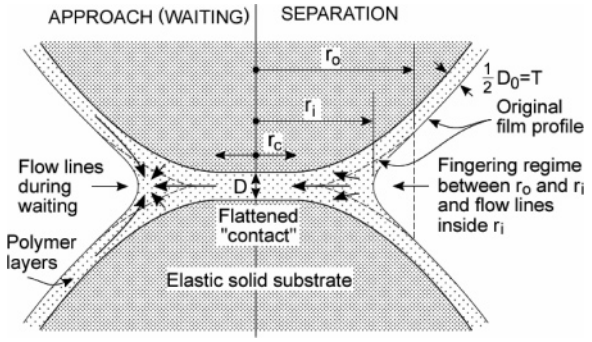

Figure 12. Local geometry of contact junction on approach and separation, showing the likely flow lines of polymer in each case. The inward viscous fingering on separation, described in Figures 6 and 7, arise because the separation is essentially a radially inward peeling of the surfaces. In contrast to loading−unloading adhesion cycles, during lateral sliding at a fixed separation D the geometry, as gauged from the FECO fringes, does not appear to change.

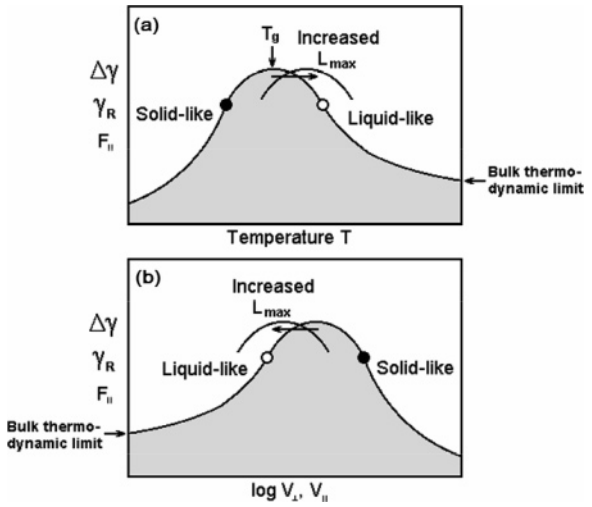

Figure 13. WLF time−temperature−load superposition representations (adhesion and friction plots) of the effects observed in this study. Note that increasing the maximum load L_{max} or pressure moves the peaks as shown; making the film more solidlike at any particular temperature or sliding velocity. Black points: glassy polymer. White points: polymer melt.

affect γ, not the bulk viscoelastic properties. In the other limit of the low MW PS 580, 700, and 800, at 10−70 °C above T_g, their behavior was fully liquidlike and governed by the bulk viscous flow behavior of the polymers. The large range of values for attaining liquidlike behavior is due to its dependence on the loading and unloading rates. Thus, for PS 580 at 23 °C (68 °C above T_g), the adhesion force tended to the thermodynamic value only for separation rates below 2.5×10^{-3} μm/s. For PS 1300 at 51 °C (∼10 °C above T_g), the same limit, based on extrapolation of the data in Figure 10b, would have been achieved at a separation rate of 10^{-6}−10^{-5} μm/s (0.01−0.1 Å/s).

With the limited data currently available on all the factors that affect adhesion and friction, we tentatively order the most important factors affecting these properties as follows: the temperature relative to T_g, followed by the loading and unloading (detachment) rates or−for the friction forces−the sliding velocity, the contact time or stopping time, followed by the film thickness (for thicknesses >30 nm or $\gg R_g$). The maximum load before separation is also important (cf. Figure 13), but more so for melts where it induces large deformations and flows. With more experiments it should be possible to fully quantify these trends.

Comparison with Previous Work on T_g in Thin Films. There are a number of different ways to measure T_g in bulk samples,[19,27−32] which can yield conflicting results, often depending on which theory or equation is used to interpret the data. Measuring the T_g of a thin film is even more complicated: additional factors such as the film thickness and segment−surface interactions affect the data, and even the concept of a uniform T_g throughout the film is highly questionable.

A number of different studies have shown both higher and lower T_g values in thin polymer films compared to the bulk T_g, usually depending on the nature of the confining surfaces.[14,33−35] Using SPM, Buenviaje et al.[35] found that a critical load and scan speed were needed to obtain accurate glass transition temperature measurements of ultrathin PS films spin-coated on a silicon surface. They also found that the T_g depends on the film thickness and that there is an increase of T_g below a critical thickness (150 nm for PS 90 000). In our study, most of the PS films had thicknesses in the range 20−200 nm (although film thicknesses up to a few microns were also studied). Our results that the T_g of thin (<100 nm thick) PS films under high loads is a few degrees higher than the bulk T_g is consistent with Buenviaje et al's result.[35]

Fingering Instabilities. Saffman and Taylor[36] showed that a moving horizontal interface between two fluids where fluid 2 pushes fluid 1 upward at a speed V (as in a vertical Hele−Shaw cell experiment), the interface becomes unstable when

$$V > (\rho_2 - \rho_1)b^2 g/12(\eta_1 - \eta_2) \tag{14}$$

where ρ_i and η_i ($i = 1,2$) are the densities and shear viscosities of the fluids and b is the distance between the two parallel plates. Gravity tends to stabilize the instability when $\rho_2 > \rho_1$, and the instability occurs only for $\eta_1 > \eta_2$. When the plates are horizontal, as is the geometry in SFA experiments, there is no gravity term, and according to eq 14, the interface is always unstable when the less viscous fluid is driving the more viscous fluid.[36] The SFA geometry can be considered as a miniature horizontal Hele−Shaw cell in which the width ($2r_0$ in Figure 12) is much greater than the channel thickness D, so that the interface is locally a straight line. Thus, in the SFA geometry and configuration, when the two surfaces are pushed together and there is an outward flow of polymer (see Figure 1 or 12), a more viscous fluid may be considered to be pushing a less viscous one, namely air. However, the reverse occurs on separation when we might expect that fingering instabilities will occur for all the polymers separations in our two systems. This is what we observed with all the low-MW polymer samples at temperatures where they could be considered as fluid (above T_g).

Chuoke et al.[37] concluded that an instability is present for all wavelengths greater than λ_c at an initially planar (horizontal) interface between two immiscible fluids where fluid 2 pushes fluid 1 upward at a speed V. For this parallel-plate geometry

$$\lambda_c = 2\pi\sqrt{\gamma b^2/12(\eta_1 - \eta_2)(V - V_c)} \tag{15}$$

In our case, $V_c = 0$, so that the minimum wavelength is

$$\lambda_c = 2\pi\sqrt{\gamma b^2/12V(\eta_1 - \eta_2)} \tag{16}$$

On the basis of eq 16, for our experimental geometry, λ_c is therefore expected to be several micrometers, which is consistent with the wavelength of the fingers as shown in Figure 6k.

CDV

Interestingly, the above analysis suggests that while for straight interfaces fingering will always occur (if $\eta_1 > \eta_2$), for circular bridges of radius r it will occur only if $\lambda < r$. This is consistent with the lack of any reports of fingering instabilities in narrow low-viscosity liquid bridges as they thin.

Comparison with Previous Work on Fingering and Cavitation Instabilities. Fingering and cavitation instabilities are very common in adhesive failure.[20,38−46] Recent work by Ben Amar,[38] Croby,[40] Derks,[46] Creton,[20,39,40,42,46] Leibler,[39,41] Poivet,[43,44] Shull,[20,40,42] Tirumkudulu,[45] and their co-workers focused on these instabilities during the separation and debonding process of two rigid plane parallel plates with a fluid film initially filling the gap between them (probe-tack geometry or flat-punch geometry). Typical force and separation distance relationships were studied both experimentally and theoretically.[43−46] The experimental results for the force vs separation shown in Figures 2 and 3 of ref 44 and Figures 3−5 of ref 46 (see also refs 43 and 45) are qualitatively very similar to those obtained here in the positive force part of the SFA "crossed cylinder" geometry (Figure 9a).

As mentioned above, theoretical predictions on the force−separation relationship in the SFA geometry have been made by Francis and Horn.[26] However, the model assumed rigid nondeforming surfaces with a liquid bridge between them, i.e., no adhesive failure such as cavitation or fingering.[26] Our elastic (deformable) surfaces and the occurrence of fingering and cavitation are the likely reasons for the "velocity weakening" effect observed, viz. $\gamma_R \propto V_\perp{}^n$ with $n = 0.15-0.36$, rather than the theoretical value of $n \approx 0.5$.

The complex and changing geometries of the deforming surfaces and liquid bridge make it difficult to define and/or measure a shear rate and Deborah number, which change by orders of magnitude during the final stages of detachment (pull-off), as shown in Figure 9b,c.

Despite the different geometries and conditions, there are many similarities between the previous probe-tack studies and our SFA results. For example, (i) cavitation always occurs at higher strain rates and is preceded by fingering, and (ii) there is always a peak in the force during the separation. However, there are also some differences due to the curved and deformable substrate geometry in the SFA experiments vs the flat and rigid geometry in the probe-tack experiments.[20,38−46] Thus, (i) $\dot{D}$ varies with time in the former but is constant and equal to the applied driving velocity $V_\perp$ in the latter, and (ii) the length scales such as the fluid film thicknesses and contact areas are typically much smaller in SFA experiments. These differences give rise to some differences in the effects and types of phenomena observed, for example, in the SFA experiments the maximum force always occurs at $\dot{D} \approx V_\perp$ (cf. Figure 9c), while in the probe-tack studies $\dot{D}$ is usually fixed and equal to $V_\perp$ at all times during the separation because of the rigid substrates used.

Implications for Material Failure Mechanisms (Cracks, Fracture, etc.). The transition from fluidlike to solidlike adhesion and friction should mirror similar transitions in material failure mechanisms, commonly referred to as mode I and mode II, respectively. For polymers in the fluid state we find that the contact geometry, i.e., the shape of the polymer surface, is everywhere "rounded", on both approach and separation (including the fingering instabilities). This geometry is similar to that proposed by theories and models of adhesion and cracks such as the JKR and the Griffith theories, which apply to ductile materials. In contrast, for hard and brittle materials the adhesion and crack junctions are believed to be "sharp" and are now described by the Hertz, Derjaguin−Muller−Toporov (DMT), and the Barrenblatt−Dugdale−Maugis theories. Further work is needed to establish the types of deformations that occur during the adhesive and shear failure of glassy and elastomeric polymers and how similar these failure mechanisms are to those of nonpolymeric solids such as metals.

Acknowledgment. This work was supported by the Department of Energy under Grant DE-FG02-87ER45331. The work on the liquid films was supported by NASA Grant NNC04GA58G.

References and Notes

(1) Chen, N. H.; Maeda, N.; Tirrell, M.; Israelachvili, J. *Macromolecules* **2005**, *38*, 3491−3503.
(2) Maeda, N.; Chen, N. H.; Tirrell, M.; Israelachvili, J. N. *Science* **2002**, *297*, 379−382.
(3) Johnson, K. L.; Kendall, K.; Roberts, A. D. *Proc. R. Soc. London, Ser. A* **1971**, *324*, 301.
(4) Bhushan, B. *Springer Handbook of Nanotechnology*; Springer-Verlag: Berlin, 2003.
(5) Chen, Y. L.; Helm, C. A.; Israelachvili, J. N. *J. Phys. Chem.* **1991**, *95*, 10736−10747.
(6) Yamada, S.; Israelachvili, J. *J. Phys. Chem. B* **1998**, *102*, 234−244.
(7) Israelachvili, J. N.; Chen, Y. L.; Yoshizawa, H. *J. Adhes. Sci. Technol.* **1994**, *8*, 1231−1249.
(8) Szoszkiewicz, R.; Bhushan, B.; Huey, B. D.; Kulik, A. J.; Gremaud, G. *J. Chem. Phys.* **2005**, 122.
(9) Israelachvili, J. N. *Intermolecular and Surface Forces*, 2nd ed.; Academic Press: Amsterdam, 1992.
(10) Oneill, M. E. *Mathematika* **1967**, *14*, 170.
(11) Oneill, M. E.; Stewarts, K. *J. Fluid Mech.* **1967**, *27*, 705.
(12) Goldman, A. J.; Cox, R. G.; Brenner, H. *Chem. Eng. Sci.* **1967**, *22*, 637.
(13) Chan, D. Y. C.; Horn, R. G. *J. Chem. Phys.* **1985**, *83*, 5311−5324.
(14) DeMaggio, G. B.; Frieze, W. E.; Gidley, D. W.; Zhu, M.; Hristov, H. A.; Yee, A. F. *Phys. Rev. Lett.* **1997**, *78*, 1524−1527.
(15) Wu, S. *Polymer Interface and Adhesion*; M. Dekker: New York, 1982.
(16) Krevelen, D. W. V. *Properties of Polymers: Their Correlation with Chemical Structure, Their Numerical Estimation and Prediction from Additive Group Contributions*, 3rd completely rev. ed.; Elsevier: Amsterdam, 1990.
(17) Li, L.; Mangipudi, V. S.; Tirrell, M.; Pocius, A. V. In *Fundamentals of Tribology and Bridging the Gap Between the Macro- and Micro/Nanoscales*; Bhushan, B. E., Ed.; Kluwer Academic Publishers: Dordrecht, 2001; pp 305−329.
(18) Brandrup, J.; Immergut, E. H. *Polymer Handbook*, 3rd ed.; Wiley: New York, 1989.
(19) Fox, T. G.; Flory, P. J. *J. Polym. Sci.* **1954**, *14*, 315−319.
(20) Shull, K. R.; Creton, C. *J. Polym. Sci., Part B: Polym. Phys.* **2004**, *42*, 4023−4043.
(21) Santangelo, P. G.; Roland, C. M. *Macromolecules* **1998**, *31*, 4581−4585.
(22) Ferry, J. *Viscoelastic Properties of Polymers*, 3rd ed.; Wiley: New York, 1980.
(23) Muller, V. M. *Colloid J.* **1996**, *58*, 612−619.
(24) Li, L. H.; Tirrell, M.; Korba, G. A.; Pocius, A. V. *J Adhes.* **2001**, *76*, 307−334.
(25) Barthel, E.; Roux, S. *Langmuir* **2000**, *16*, 8134−8138.
(26) Francis, B. A.; Horn, R. G. *J. Appl. Phys.* **2001**, *89*, 4167−4174.
(27) Fox, T. G.; Flory, P. J. *J. Phys. Chem.* **1951**, *55*, 221−234.
(28) Fox, T. G.; Flory, P. J. *J. Appl. Phys.* **1950**, *21*, 581.
(29) Marzio, E. A. D.; Gibbs, J. H. *J. Chem. Phys.* **1958**, *28*, 807.
(30) Gibbs, J. H.; Marzio, E. A. D. *J. Chem. Phys.* **1958**, *28*, 373.
(31) Gibbs, J. H. *J. Chem. Phys.* **1956**, *25*, 185.
(32) Kovacs, J.; Aklonis, J. J.; Hutchinson, J. M.; Ramos, R. J. *J. Polym. Sci., Polym. Phys. Ed.* **1979**, *17*, 1097.
(33) Mayes, A. M. *Macromolecules* **1994**, *27*, 3114−3115.
(34) Wallace, W. E.; Vanzanten, J. H.; Wu, W. L. *Phys. Rev. E* **1995**, *52*, 3329−3332.
(35) Buenviaje, C.; Dinelli, F.; Overney, R. M. In *Glass Transition Measurements of Ultrathin Polystyrene Films*; *ACS Symp. Ser.* **2000**, *781*, 76−92.
(36) Saffman, P. G.; Taylor, G. *Proc. R. Soc. London, Ser. A* **1958**, *245*, 312.
(37) Chuoke, R. L.; Vanmeurs, P.; Vanderpoel, C. T. *Am. Inst. Min. Metall. Eng.* **1959**, *216*, 188−194.
(38) Ben Amar, M.; Bonn, D. *Physica D* **2005**, *209*, 1−16.
(39) Creton, C.; Leibler, L. *J. Polym. Sci., Part B: Polym. Phys.* **1996**, *34*, 545−554.

(40) Crosby, A. J.; Shull, K. R.; Lakrout, H.; Creton, C. *J. Appl. Phys.* **2000**, *88*, 2956−2966.
(41) Gay, C.; Leibler, L. *Phys. Rev. Lett.* **1999**, *82*, 936−939.
(42) Lakrout, H.; Creton, C.; Ahn, D. C.; Shull, K. R. *Macromolecules* **2001**, *34*, 7448−7458.
(43) Poivet, S.; Nallet, F.; Gay, C.; Fabre, P. *Europhys. Lett.* **2003**, *62*, 244−250.
(44) Poivet, S.; Nallet, F.; Gay, C.; Teisseire, J.; Fabre, P. *Eur. Phys. J. E* **2004**, *15*, 97−116.
(45) Tirumkudulu, M.; Russel, W. B.; Huang, T. *J. Phys. Fluids* **2003**, *15*, 1588−1605.
(46) Derks, D.; Lindner, A.; Creton, C.; Bonn, D. *J. Appl. Phys.* **2003**, *93*, 1557−1566.
(47) According to the Saffman-Taylor instability mechanism, no fingering is expected when a high-viscosity front is displacing a lower-viscosity front, as is the case on loading where the displaced "fluid" is air. The reverse is true on unloading, where fingering is always expected (see Discussion).
(48) Another definition of the Deborah number in ref 42 uses the initial gap distance D_0 instead of the (varying) D; i.e., the denominator is constant.
(49) A peak in γ_R usually reflects a peak in the adhesion energy hysteresis, $\Delta\gamma = (\gamma_R - \gamma_A)$, because the advancing or loading energy γ_A is usually much lower and close to the thermodynamic value, γ_0 (cf. Figure 8 and ref 1). Thus, when $\gamma_R \gg \gamma_A$, we may write $\Delta\gamma \approx \gamma_R$.
(50) Below the critical velocity the polymers become Newtonian liquids where γ_R equals the bulk value which no longer changes with the separation velocity $V_\perp$ (cf. Figure 2).

MA052207O